

Something something something physics

Steven Green
of Emmanuel College

A dissertation submitted to the University of Cambridge
for the degree of Doctor of Philosophy

Abstract

This thesis describes the optimisation of the calorimeter design for collider experiments at the future Compact Linear Collider (CLIC) and the International Linear Collider (ILC). The detector design of these experiments is built around high-granularity Particle Flow Calorimetry that, in contrast to traditional calorimetry, uses the energy measurements for charged particles from the tracking detectors. This can only be realised if calorimetric energy deposits from charged particles can be separated from those of neutral particles. This is made possible with fine granularity calorimeters and sophisticated pattern recognition software, which is provided by the PandoraPFA algorithm. This thesis presents results on Particle Flow calorimetry performance for a number of detector configurations. To obtain these results a new calibration procedure was developed and applied to the detector simulation and reconstruction to ensure optimal performance was achieved for each detector configuration considered.

This thesis also describes the development of a software compensation technique that vastly improves the intrinsic energy resolution of a Particle Flow Calorimetry detector. This technique is implemented within the PandoraPFA framework and demonstrates the gains that can be made by fully exploiting the information provided by the fine granularity calorimeters envisaged at a future linear collider.

A study of the sensitivity of the CLIC experiment to anomalous gauge couplings that effect vector boson scattering processes is presented. These anomalous couplings provide insight into possible beyond standard model physics. This study, which utilises the excellent jet energy resolution from Particle Flow Calorimetry, was performed at centre-of-mass energies of 1.4 TeV and 3 TeV with integrated lumi-

nosities of 1.5ab^{-1} and 2ab^{-1} respectively. The precision achievable at CLIC is shown to be approximately one to two orders of magnitude better than that currently offered by the LHC.

Finally, a study into various technology options for the CLIC vertex detector is described.

Declaration

This dissertation is the result of my own work, except where explicit reference is made to the work of others, and has not been submitted for another qualification to this or any other university. This dissertation does not exceed the word limit for the respective Degree Committee.

Andy Buckley

Acknowledgements

Of the many people who deserve thanks, some are particularly prominent, such as my supervisor...

Preface

This thesis describes my research on various aspects of the LHCb particle physics program, centred around the LHCb detector and LHC accelerator at CERN in Geneva.

For this example, I'll just mention Chapter ?? and Chapter ??.

Contents

1. Calorimeter Optimisation Studies	1
1.1. Calorimeter Optimisation Studies	1
1.2. Metric	2
1.3. Simulation and Reconstruction	2
1.4. Calibration	2
1.5. Nominal Detector Performance	2
1.6. Electromagnetic Calorimeter Optimisation	3
1.6.1. ECal Transverse Granularity	4
1.6.2. ECal Longitudinal Granularity	6
1.6.3. ECal Active Material	9
1.7. Hadronic Calorimeter Optimisation	10
1.7.1. HCal Absorber Material	11
1.7.2. HCal Transverse Granularity	13
1.7.3. HCal Longitudinal Granularity	15
1.7.4. HCal Sampling Fraction	15
1.7.5. HCal Sampling Frequency	15
1.8. Global Detector Parameters	18
A. Pointless extras	19
A.1. Anomalous Gauge Coupling Quartic Vertices Of Relevance in Vector Boson Scattering	19
A.2. χ^2 Contour Plots for Jet Algorithm Optimisation	22
Bibliography	27
List of figures	29
List of tables	31

*“Writing in English is the most ingenious torture
ever devised for sins committed in previous lives.”*

— James Joyce

Chapter 1.

Calorimeter Optimisation Studies

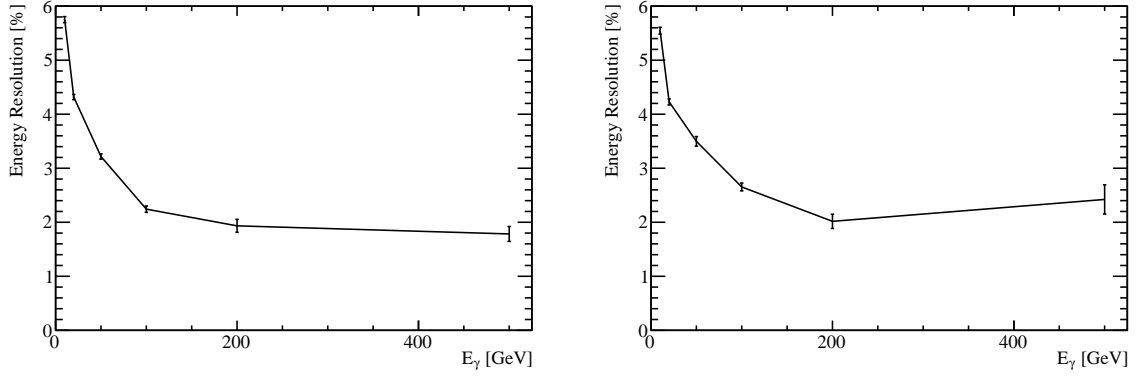
“There, sir! that is the perfection of vessels!”

— Jules Verne, 1828–1905

1.1. Calorimeter Optimisation Studies

If the future linear collider is to reach it’s maximum potential in terms of energy resolution then, optimisation of the detector will be essential. The energy resolution in the particle flow paradigm is dependant upon several detector components. The momentum of charged particles arises from the shape of the tracks deposited within the detector while the energy of uncharged particles arise from calorimetric measurements. Application of sophisticated pattern recognition algorithms allows the particle type to be inferred for the charged particles. In tern this allows for the conversion of the track momentum into an energy measure for the charged particles. The particle identification algorithms use the topological information acquired from the calorimetric energy deposited to infer particle type for a subset of charged particles.

The calorimetric energy deposits are therefore used in a twofold manner: (i) as energy measurements for neutral particles and (ii) as input for particle identification algorithms. There is potential for significant gains to be made in physics performance by optimising the calorimeters due to their dominant role in energy measurements. In this chapter the optimisation of the calorimeters is considered. Parameters such



(a) Silicon active material, $5 \times 5\text{mm}^2$ ECal transverse granularity. **(b)** Scintillator active material, $5 \times 5\text{mm}^2$ ECal transverse granularity.

Figure 1.1.: Energy resolution as a function of photon energy for the nominal ILD detector for both the silicon and scintillator options.

as the longitudinal granularity, transverse granularity and material choices for the calorimeters are considered.

This chapter concludes with an optimisation of several global parameters for the detector. These parameters are not calorimeter specific, but the optimisation procedure developed for the calorimeters is appropriate to use. These parameters relate to the global detector size and the magnetic field applied throughout solenoid in the detector.

1.2. Metric

1.3. Simulation and Reconstruction

1.4. Calibration

1.5. Nominal Detector Performance

The energy resolution for single photon events as a function of photon energy, for the nominal ILD detector, is shown in figure 1.1. The nominal jet energy resolution can be found in section BLAH.

1.6. Electromagnetic Calorimeter Optimisation

The ECal primarily measures the energy deposits of electromagnetic showers. The default ILD detector model ECal, summarised in table 1.1, contains 24 radiation lengths (X_0 , which acts to confine all but the highest energy electromagnetic showers within it. The longitudinal structure of this default model is 29 readout layers, consisting of pairs of active and absorber material, and one presampling layer, which exists to encourage shower development. Increasing the thickness of the absorber material part way into the detector reduces the number of readout channels and cost of the overall calorimeter while retaining a high sampling rate at the start of particle showers, which is crucial for the pattern recognition aspect of particle flow calorimetry.

Parameter	Default Value
Transverse Granularity	$5 \times 5 \text{ mm}^2$ square cells
Longitudinal Granularity	29 Readout Layers, 1 Presampling Layers
Active Material Choice	Silicon or Scintillator
Active Material Thickness	0.5 mm (Silicon) or 2 mm (Scintillator)
Absorber Material Choice	Tungsten
Absorber Material Thickness	20 Layers of 2.1 mm followed by 9 Layers of 4.2 mm

Table 1.1.: Nominal ILD detector model ECal configuration.

The parameters being optimised in this study are:

- Transverse granularity or cell size. This is a vital aspect of the detector in the particle flow paradigm as smaller cell sizes give greater potential for being able to separate energy deposits from charged and neutral particles. This transverse granularity should have little to no effect on the intrinsic energy resolution of the detector.
- Longitudinal granularity or cell depth. This parameter dictates the intrinsic energy resolution of the detector as smaller cell depths mean more sampling is done of the particle shower and so, due to the Poissonian statistics governing the measurement of particle showers, the better the resolution.
- Active material choice. This is a choice between silicon or scintillator. As well as providing different intrinsic energy resolutions the readout mechanics of these

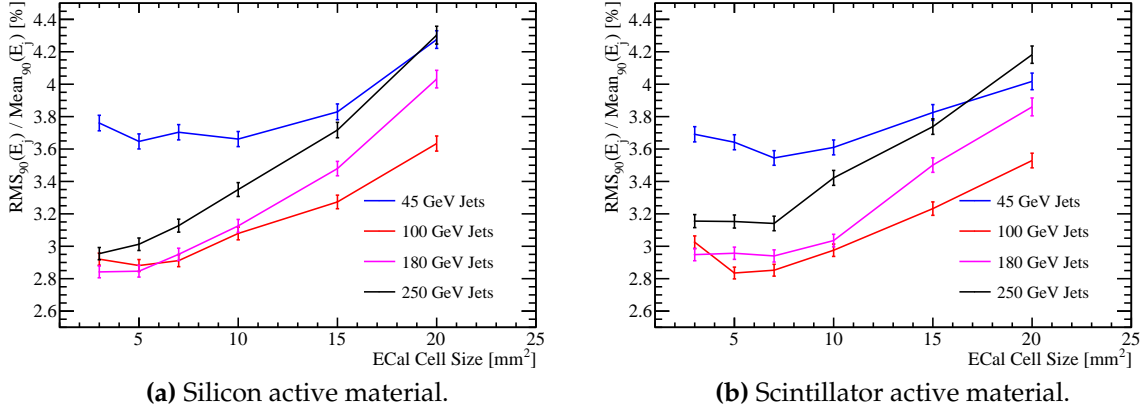


Figure 1.2.: Jet energy resolution as a function of ECal cell size for the silicon and scintillator ECal options.

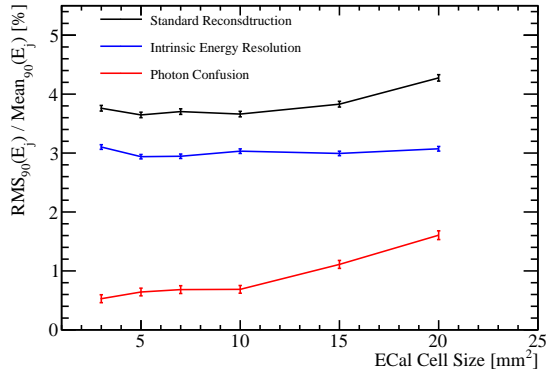
two options are significantly different. There is no clear prior knowledge as to which should provide better performance.

1.6.1. ECal Transverse Granularity

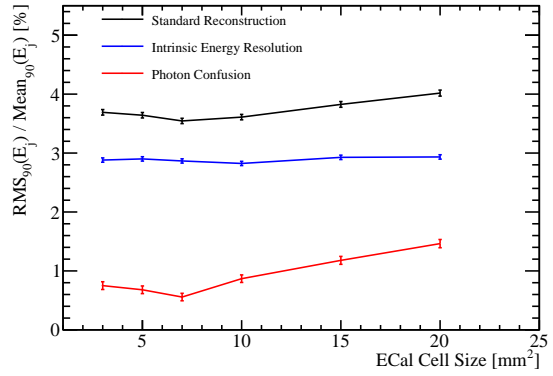
For this study a number of different detector models were considered where the transverse granularity in the ECal had been varied about the nominal value of $5 \times 5 \text{ mm}^2$ square cells. The granularities considered were $3 \times 3 \text{ mm}^2$, $5 \times 5 \text{ mm}^2$, $7 \times 7 \text{ mm}^2$, $10 \times 10 \text{ mm}^2$, $15 \times 15 \text{ mm}^2$ and $20 \times 20 \text{ mm}^2$ square cells for both the silicon and scintillator active material options. The jet energy resolution as a function of transverse granularity in the ECal is shown in figure 1.2.

The jet energy resolution was found to improve with decreasing cell size. This is expected as smaller cell size lead to better separation of energy deposits from neutral and charged particle showers.

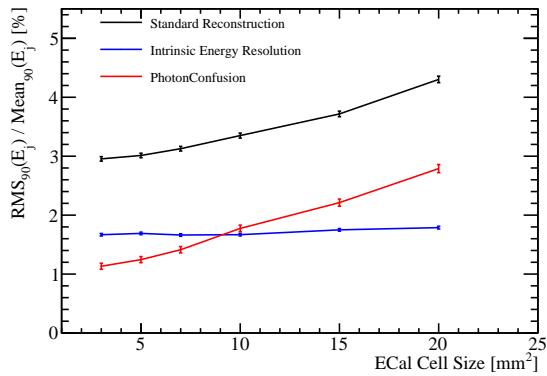
By examining the breakdown of the jet energy resolution into intrinsic resolution and confusion terms, as explained in chapter BLAH, it is possible to conclude that the dominant factor affecting the jet energy resolution when the transverse granularity of the ECal is varied is the confusion arising from photon energy deposits. Examples of jet energy resolution breakdowns are shown for 45 and 250 GeV jets for both the silicon and scintillator ECal options in figure 1.3. As expected in the intrinsic energy resolution does not change significantly with the transverse granularity.



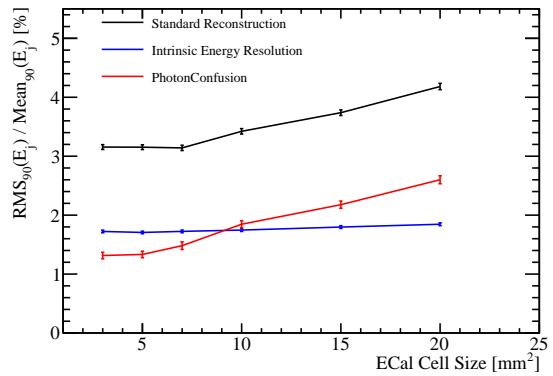
(a) Silicon active material, 45 GeV Jets.



(b) Scintillator active material, 45 GeV Jets.



(c) Silicon active material, 250 GeV Jets.



(d) Scintillator active material, 250 GeV Jets.

Figure 1.3.: Jet energy resolution breakdown as a function of ECal transverse granularity for 45 and 250 GeV jets. Results are given for both the silicon and scintillator ECal options.

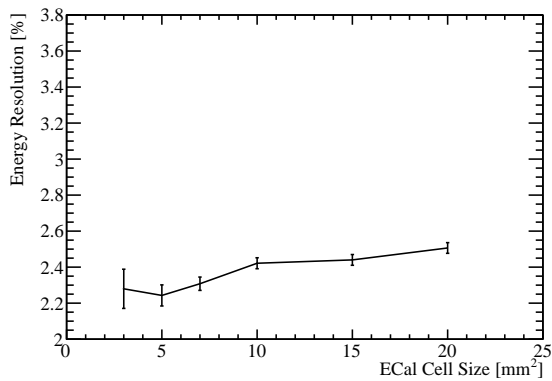
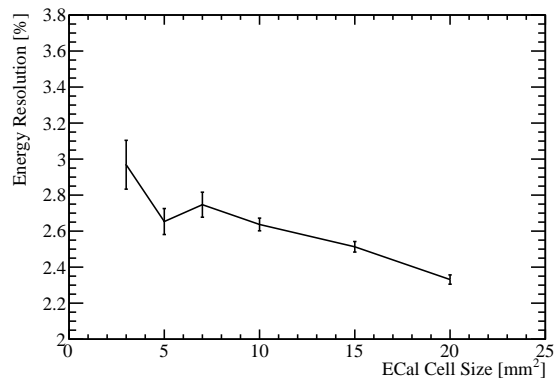
(a) Silicon active material, 100 GeV γ .(b) Scintillator active material, 100 GeV γ .

Figure 1.4.: Energy resolution as a function of ECal transverse granularity for 100 GeV photons. Results are given for both the silicon and scintillator ECal options.

A more targeted test of the intrinsic energy resolution of the ECal is presented in figure 1.4, which examines the energy resolution of single photon samples at 100 GeV. For the silicon option the intrinsic energy resolution was found to not vary significantly across the transverse granularities under consideration, however, there is a degradation in energy resolution with increasing cell size for the scintillator option. This originates from an inactive region of material in the simulation that represents the multi pixel photon counter (MPPC). The MPPC occupies a fixed area of the cell irrespective of cell size and so fractionally the "dead" region of the cell increases as cell size is reduced (cite this somehow). These trends will be present in the jet energy resolution studies, however, as only a small fraction, $\approx 10\%$, of the jet energy arises from the ECal these trends will be washed out when looking purely at jets.

In conclusion smaller transverse granularities in the ECal significantly improve the jet energy resolution for both the silicon and scintillator options. The intrinsic energy resolution of the ECal is largely invariant to changes in the transverse granularity for the silicon option, while larger transverse granularities are beneficial to the scintillator option as they reduce the impact of "dead" regions of the detector.

1.6.2. ECal Longitudinal Granularity

The performance of a number of detector configurations was examined where the longitudinal granularity of the ECal absorber material had been varied about the nominal value. This study was performed for both the silicon and scintillator active material options. In all cases considered tungsten was used as the absorber material in the ECal and the active layer thicknesses were not changed, that is 0.5 mm for the silicon option and 2 mm for the scintillator option. The layout of the ECal for detector models considered are summarised in table 1.2. For each detector model considered in this study the total number of radiation lengths in the ECal is kept approximately constant. This is done by varying the thickness of the absorber material when modifying the number of layers in the ECal.

The jet energy resolution was found to improve with increasing longitudinal granularity. This is expected as a more layers in the calorimeter, for the same total thickness, implies greater sampling of the particle shower and so, as the energy resolution obeys Poissonian statistics, an improvement in the intrinsic energy resolution is observed.

Total Number of Layers $N_{\text{Layers ECal}}$	N_{Layers} Region 1	Absorber Thickness Region 1 [mm]	N_{Layers} Region 2	Absorber Thickness Region 2 [mm]	Total Thickness [X_0]
30	20	2.10	9	4.20	22.77
26	17	2.40	8	4.80	22.60
20	13	3.15	6	6.30	22.47
16	10	4.00	5	8.00	22.31

Table 1.2.: Transverse granularity layout of various ECal models considered in this study. Radiation length of tungsten absorber is 3.504mm [2]. Note that the presampler layer contributes one layer to the cumulative number of layers value for all detector models considered.

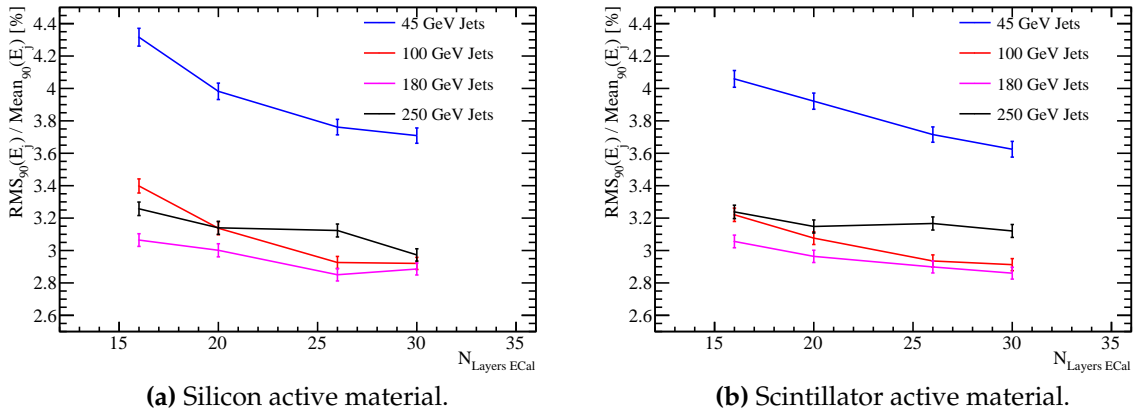
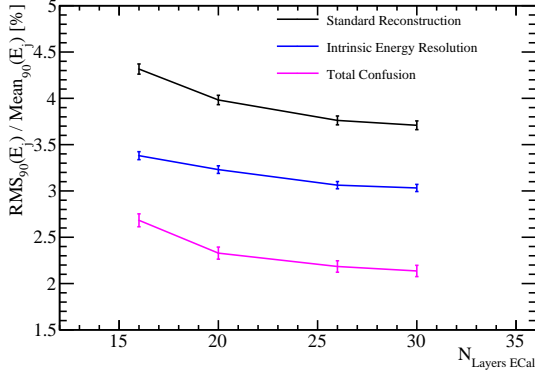


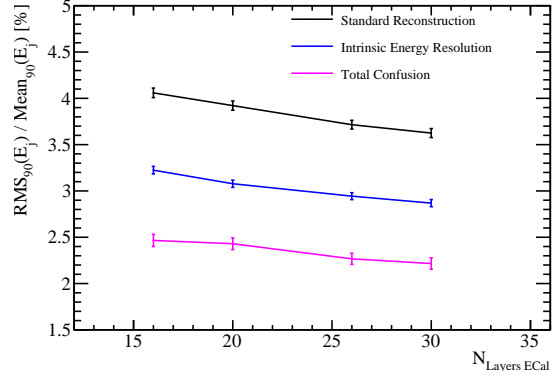
Figure 1.5.: Jet energy resolution as a function of longitudinal granularity in the ECal for the silicon and scintillator ECal options.

A particularly strong dependancy on ECal longitudinal granularity is noted at low energies, but this reduces significantly as energies rise.

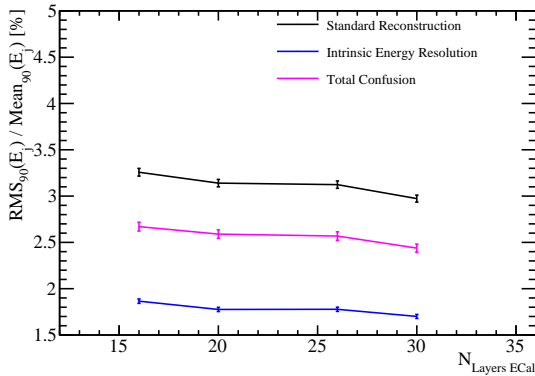
The strong dependancy of the jet energy resolution on the ECal longitudinal granularity can be expanded upon by looking at the decomposition of the jet energy resolution, which is shown in figure 1.6 for the 45 and 250 GeV energy jets. At low energies the trend is twofold: an improvement to the intrinsic energy resolution with more sampling of particle showers and a reduction in the impact of confusion. For high energy jets, where confusion dominates, there is little to no change in the intrinsic energy resolution and confusion as a function of ECal transverse granularity.



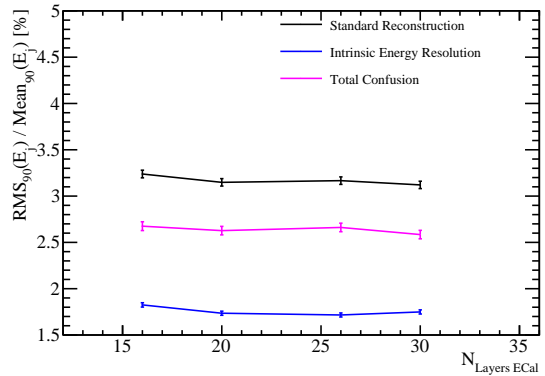
(a) Silicon active material, 45 GeV Jets.



(b) Scintillator active material, 45 GeV Jets.



(c) Silicon active material, 250 GeV Jets.



(d) Scintillator active material, 250 GeV Jets.

Figure 1.6.: Jet energy resolution breakdown as a function of ECal longitudinal granularity for 45 and 250 GeV jets. Results are given for both the silicon and scintillator ECal options.

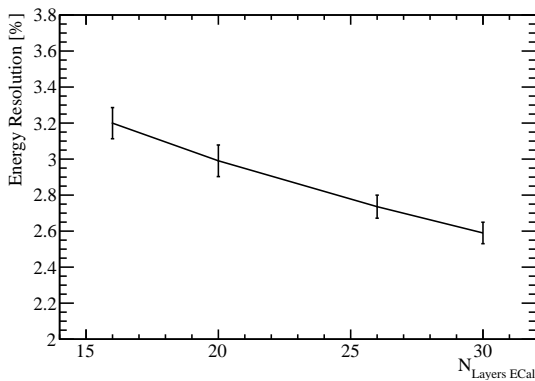
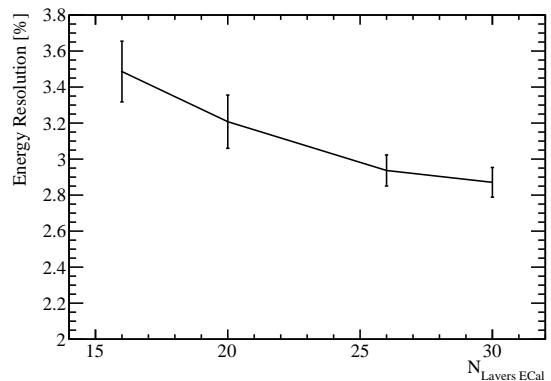
(a) Silicon active material, 100 GeV γ .(b) Scintillator active material, 100 GeV γ .

Figure 1.7.: Energy resolution as a function of function of ECal longitudinal granularity for 100 GeV photons. Results are given for both the silicon and scintillator ECal options.

Further understanding is gained by considering the energy resolution of single photon samples at 100 GeV as a function of the longitudinal granularity in the ECal, which is shown in figure 1.7. At these large photon energies it is clear that the intrinsic energy resolution of the ECal is improved by having finer longitudinal segmentation in the ECal. This trend will be present in the jet energy resolution study, but as only $\approx 10\%$ of the jet energy is measured in the ECal in comparison to $\approx 100\%$ of the photons energy, it will be obscured by the energy resolution of the rest of the detector, which is invariant to the ECal longitudinal segmentation.

The intrinsic energy resolution of the ECal is improved by having a finer transverse granularity. This is evident when looking at the energy resolution of photons whose energy deposits are localised within the ECal. This trend is again clear when considering the energy resolution of low energy jets, however, at higher energies the longitudinal granularity in the ECal is not a significant factor in determining detector performance.

1.6.3. ECal Active Material

In sections 1.6.1 and 1.6.2 the performance of the ECal was reported for both the silicon and scintillator options and to a large extent the performance of the two options was the same. There were a few differences, which attention should be brought to:

- The intrinsic energy resolution of a silicon ECal is worse than that of a scintillator ECal for low energies, while the trend is reversed at high energies. The cross over point in performance occurs between 20 and 50 GeV. This trend is shown in figure 1.1.
- The "dead" region due to the presence of the MPPC in the scintillator option degrades performance of the detector for small transverse granularities. No such effect is seen for the silicon option. This effect is shown in figure 1.4.

The lack of this "dead" region of the detector and the beneficial intrinsic energy resolution at large energies indicates a preference for a silicon detector, however, there is no clear preference based on these studies.

1.7. Hadronic Calorimeter Optimisation

The HCal is designed to measure the energy deposits from hadrons. The default ILD detector model HCal, summarised in table 1.3, contains ≈ 6 nuclear interaction lengths (λ_I). The ECal contributes approximately one λ_I giving a total of $\approx 7\lambda_I$, which is sufficient to confine the bulk of jets up to 1 TeV events, which is the maximum running energy for the ILC. The longitudinal structure of this model consists of 48 readout layers each containing a 3 mm active layer of scintillator and a 20 mm absorber layer of iron. There are several readout technology options under consideration for the HCal, which are analogue, digital and semi-digital, however, for this study only the analogue HCal is considered.

Parameter	Default Value
Transverse Granularity	$30 \times 30\text{mm}^2$ square cells
Longitudinal Granularity	48 Readout Layers
Active Material Choice	Scintillator Tiles
Active Material Thickness	3 mm
Absorber Material Choice	Steel
Absorber Material Thickness	20 mm

Table 1.3.: Nominal ILD detector model HCal configuration.

The parameters being optimised in this study are:

- Transverse granularity or cell size. This is key to successful application of pattern recognition in the particle flow paradigm, but should not change intrinsic energy resolution.
- Longitudinal granularity or cell depth. This governs the intrinsic energy resolution of a calorimeter.
- Depth of calorimeter. This is important in determining the impact of leakage of energy out of the detector.
- Sampling fraction. This is the ratio of the active medium thickness to the absorber medium thickness. As sampling calorimetry is based on sampling of particle showers it is expected that this is an important parameter. However, above a given sampling fraction there should be little difference between performance if

showers are sampled at a high enough rate to get a good estimate of the incoming particles energy.

- Absorber material choice. This is a choice between steel or tungsten. While this does not change the active medium choice it does dictate the growth and propagation of showers and so plays a crucial role in calorimetry. While tungsten is more expensive than steel for the raw material the larger number of interaction lengths per length scale for tungsten mean that it is possible to create a smaller detector with the same number of interaction lengths within it. This reduces the size of the solenoid needed to generate the magnetic field and so lowers the price of the detector. As both of these materials are viable as absorber medium choices it is crucial to determine if either is more advantageous from a physics perspective.

1.7.1. HCal Absorber Material

The nominal choice of absorber material is steel, tungsten provides a feasible alternative material. While more expensive than steel, tungsten contains more radiation lengths per unit length than steel and so the overall size of the detector would reduce meaning the solenoid could be smaller, which would to first order offset the additional cost of the tungsten. This section aims to determine whether either of these options is beneficial when considering the jet energy resolution of the detector.

In this study the total depth of absorber material, in nuclear interaction lengths, was held constant for both models. This was to ensure any performance changes were not due to additional material as opposed to the intrinsic energy resolutions of the absorber materials. The interaction of hadrons with the absorber material within the detector is simulated by GEANT4. The model for these interactions is dependent upon the choice of physics list, which by default is the QGSP_BERT physics list. This list is recommended by the GEANT4 authors to use for high energy physics calorimetry as it gives good agreement between experiment. For this study both the QGSP_BERT and the QGSP_BERT_HP physics lists are tested. The QGSP_BERT_HP list uses the high precision neutron package (NeutronHP) to deal with the transportation of neutrons from below 20 MeV to thermal energies. This added detail was thought to be necessary for a study involving tungsten due to the increased time of shower development.

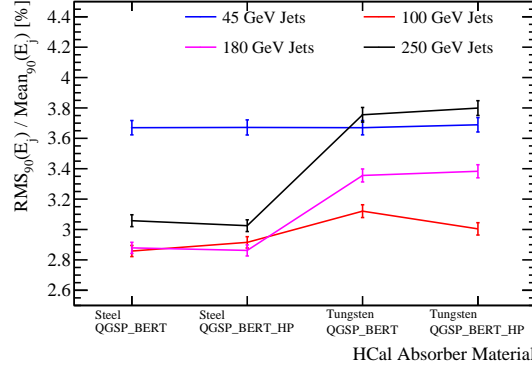


Figure 1.8.: Jet energy resolution as a function of absorber material in the HCal and physics list.

The jet energy resolution for the steel and the tungsten HCal options, for using both the QGSP_BERT and the QGSP_BERT_HP physics lists, are shown in figure 1.8. These results indicate that steel outperforms tungsten as an absorber material, particularly for high energy jets. At low energies the performance is similar, indicating that the intrinsic energy resolution of the two options is comparable. The use of the QGSP_BERT_HP physics list, as opposed to QGSP_BERT, has a minimal impact on these results.

Expanding upon this further by examining the jet energy resolution breakdowns as shown in figure 1.9, it can be seen that the change in performance when changing the HCal absorber material from steel to tungsten is due to changes in the confusion. The change in confusion is most likely due to the fact that the PandoraPFA algorithms are tuned for HCal cell dimensions based on the steel HCal option, while the HCal cells for the tungsten option HCal will be smaller by a factor of approximately 1.7 ($\approx 16.77/9.946$). The jet energy resolution breakdowns also indicate that the intrinsic energy resolution of the tungsten HCal is marginally worse, particularly for high energy jets, than that of a steel HCal. Therefore, even if the algorithms were fully optimised for the tungsten option such that the confusion terms for the two options were comparable the performance of the steel HCal would still be preferred over the tungsten option making the steel option the more preferred of the two.

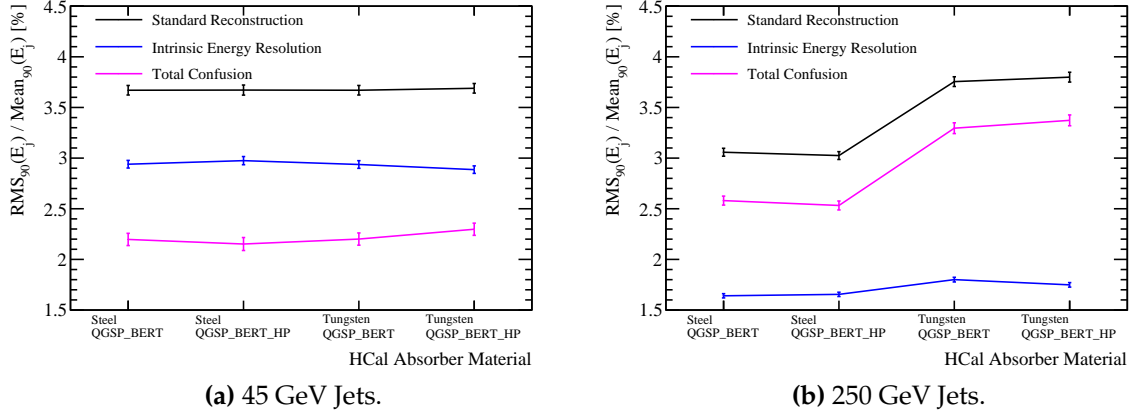


Figure 1.9.: Jet energy resolution breakdown as a function of HCal absorber material and physics list for 45 and 250 GeV jets.

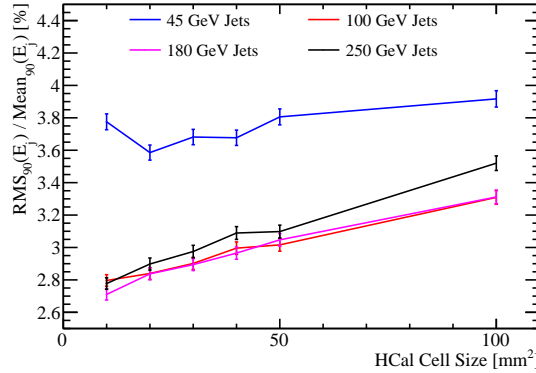


Figure 1.10.: Jet energy resolution as a function of HCal cell size.

1.7.2. HCal Transverse Granularity

For this study a number of different detector models were considered where the transverse granularity in the HCal had been varied about the nominal value of $30 \times 30 \text{ mm}^2$ square cells. The granularities considered were $10 \times 10 \text{ mm}^2$, $20 \times 20 \text{ mm}^2$, $30 \times 30 \text{ mm}^2$, $40 \times 40 \text{ mm}^2$, $50 \times 50 \text{ mm}^2$ and $100 \times 100 \text{ mm}^2$ square cells. The jet energy resolution as a function of transverse granularity in the HCal is shown in figure 1.10.

As with the case for the ECal, the jet energy resolution was found to improve with decreasing cell size as smaller cell size lead to better separation of energy deposits from neutral and charged particle showers.

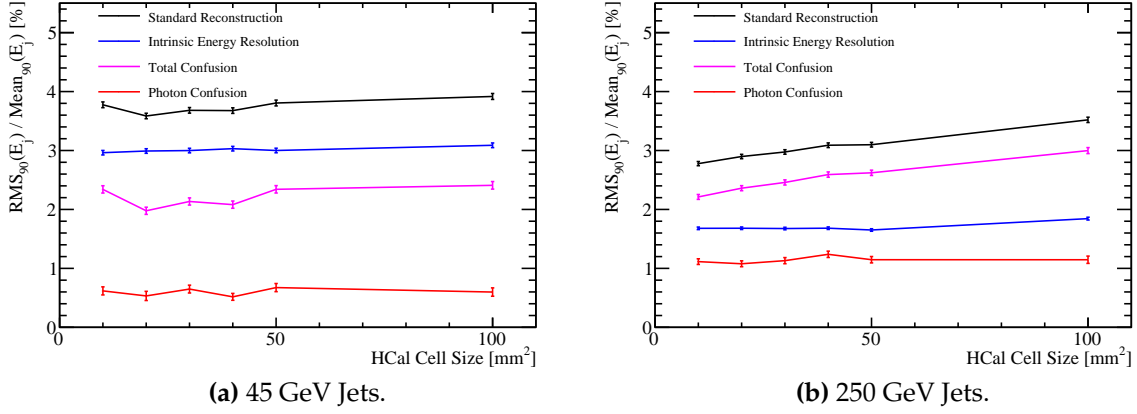


Figure 1.11.: Jet energy resolution breakdown as a function of HCal transverse granularity for 45 and 250 GeV jets.

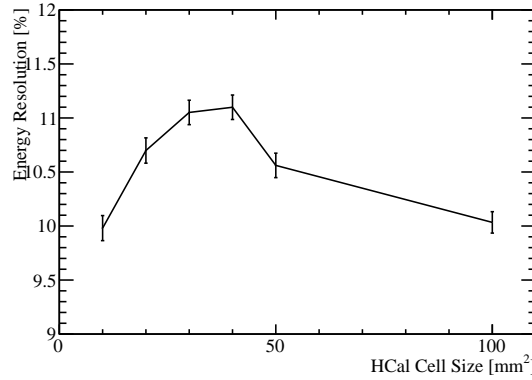


Figure 1.12.: Energy resolution as a function of HCal transverse granularity for 50 GeV K_L^0 .

The jet energy resolution breakdowns, shown in figure, 1.11, show that the confusion term varies when changing the HCal transverse granularity, but the intrinsic energy resolution does not. Furthermore, the photon confusion is invariant to changes in HCal transverse granularity, indicating that the observed overall performance changes are due to the effects of confusion arising from energy deposits from charged and neutral hadrons. Once again for 45 GeV jets the detector performance is dominated by intrinsic energy resolution and so HCal transverse granularity has little effect, while for 250 GeV jets the performance is dominated by confusion and HCal transverse granularity becomes more significant.

The energy resolution of single long lived neutral kaons, K_L^0 , at 50 GeV is considered as a function of transverse granularity in the HCal. This is shown in figure 1.12 and, as expected, the energy resolution of the detector is largely invariant to changes in

the transverse granularity in the HCal. As these K_L^0 samples may deposit energy in the ECal, this figure represents the intrinsic energy resolution of the ILD detector as a whole and not purely that of the HCal. However, it is expected that the bulk of the energy deposited by these samples occurs within the HCal and so such plots are a useful representation of the HCal performance.

The transverse granularity of the HCal acts to determine the impact of confusion from charged and neutral hadron energy deposits. It does not vary the intrinsic energy resolution of the detector, nor does it impact the reconstruction of photons. As confusion is dominant at high jet energies the HCal transverse granularity gains an increasing role in determining detector performance as the energy in an event increases.

1.7.3. HCal Longitudinal Granularity

MAKE THIS SECTION ABOUT ADDING LAYERS TO HCal

1.7.4. HCal Sampling Fraction

1.7.5. HCal Sampling Frequency

A number of detector models were examined where the longitudinal segmentation of the HCal, of fixed total thickness, had been varied about the nominal value. In all cases the absorber material was steel while the active material was scintillator. Each HCal configuration had the same total number of nuclear interaction lengths, $5.72 \lambda_I$ in the absorber material and $0.19 \lambda_I$ in the active material, however, the thickness of the layers was varied depending on the total number of layers being considered. The ratio of the active material layers to the absorber material layers, the sampling fraction, was also kept constant in this study. A summary of the detector models considered in this study can be found in table 1.4.

The jet energy resolution for the various detector models considered is shown in figure 1.15. It was found that increasing the number of layers in the HCal, for the same total thickness, improved the jet energy resolution for all jet energies considered. Based on the increase in the frequency of sampling of particle showers in the HCal, it is

Number $N_{\text{Layers HCal}}$	Absorber Thickness [mm]	Active Thickness [mm]
60	16.00	2.40
54	17.78	2.67
48	20.00	3.00
42	22.86	3.43
36	26.67	4.00
30	32.00	4.80
24	40.00	6.00
18	53.33	8.00

Table 1.4.: Transverse granularity layout of various HCal models considered.

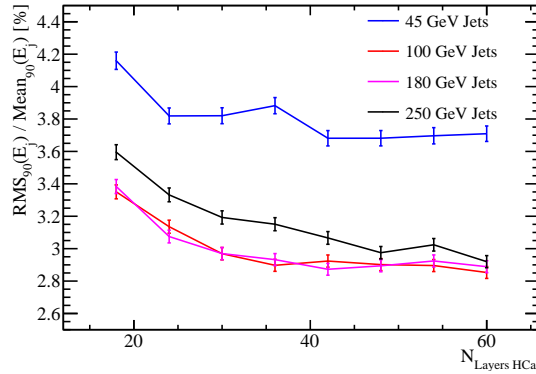


Figure 1.13.: Jet energy resolution as a function of longitudinal granularity in the HCal.

expected that the intrinsic energy resolution of the detector should improve. However, the improvement observed in jet energy resolution for high energy jets indicates that longitudinal granularity is also affecting the confusion terms.

These trends are further explored by considering the breakdown of jet energy resolution, which are shown in figure 1.14. As expected from the standard performance reconstruction trends as a function of jet energy, there is an improvement in both the intrinsic energy resolution and a reduction in the impact of confusion when the number of layers in the HCal is increased. The dominant trend driving the overall detector performance is that associated with the confusion of separating energy deposits from charged and neutral particles. This emphasises the importance of pattern recognition to detector performance in the particle flow paradigm.

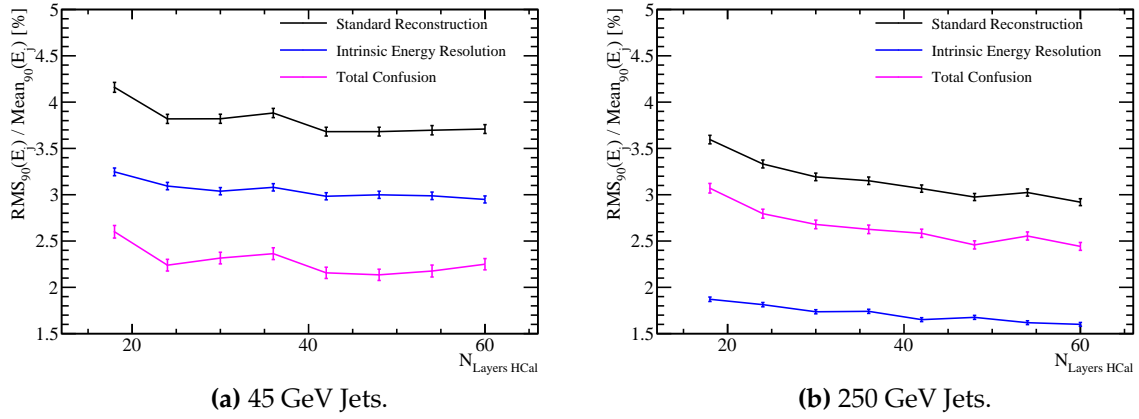


Figure 1.14.: Jet energy resolution breakdown as a function of HCal longitudinal granularity for 45 and 250 GeV jets.

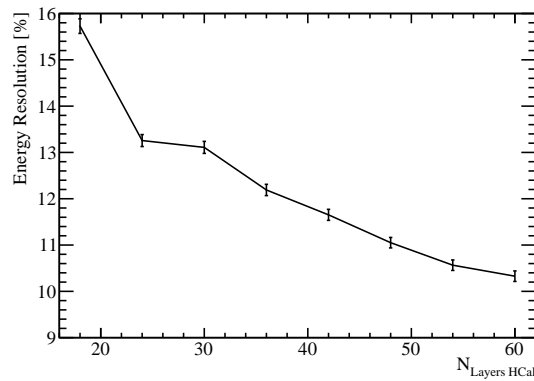


Figure 1.15.: Energy resolution as a function of HCal longitudinal granularity for 50 GeV K_L^0 .

The change in the intrinsic energy resolution of the HCal when varying the longitudinal granularity is best summarised by looking at the energy resolution of neutral hadrons as in the particle flow paradigm the energy of neutral hadrons is primarily measured in the HCal. A plot of energy resolution against the number of layers in the HCal for 50 GeV K_L^0 can be found in figure 1.15. This data shows that a reduction in sampling frequency of a particle shower that accompanies a reduction in the number of readout layers results in a broadening of energy distributions and a degradation in the resolution. It should again be emphasised that these results are for the full ILD detector model and so include the effect of the $\approx 1\lambda_I$ in the ECal.

The increasing the HCal longitudinal granularity has a twofold effect on the detector performance: an increase in sampling rate of particle showers and an improvement to the intrinsic energy resolution and a reduction in the confusion arising from associating energy deposits from hadrons.

1.8. Global Detector Parameters

Appendix A.

Pointless extras

*“Le savant n’étudie pas la nature parce que cela est utile;
il l’étudie parce qu’il y prend plaisir,
et il y prend plaisir parce qu’elle est belle.”*
— Henri Poincaré, 1854–1912

Appendixes (or should that be “appendices”?) make you look really clever, ’cos it’s like you had more clever stuff to say than could be fitted into the main bit of your thesis. Yeah. So everyone should have at least three of them...

A.1. Anomalous Gauge Coupling Quartic Vertices Of Relevance in Vector Boson Scattering

The anomalous gauge couplings involving α_4 and α_5 arise in EFT through the addition of the following terms to the Lagrangian.

$$\text{Tr}(V^\mu V_\nu) \text{Tr}(V^\nu V_\mu) \text{ and } [\text{Tr}(V^\mu V_\mu)]^2 \quad (\text{A.1})$$

Where V_μ is defined in the following way.

$$V_\mu = \Sigma(D_\mu \Sigma)^\dagger \quad (\text{A.2})$$

and Σ , the Higgs field matrix, is defined as.

$$\Sigma = \exp\left(-\frac{i}{v}\mathbf{w}\right) \quad (\text{A.3})$$

Where $\mathbf{w} = w^a \sigma^a$. w^a are the ... and σ^a are the Pauli spin matrices. The covariant derivative of the Higgs field matrix is

$$D_\mu \Sigma = \left(\partial_\mu + \frac{ig}{2}W_\mu - \frac{ig'}{2}B_\mu\sigma^3\right)\Sigma \quad (\text{A.4})$$

For clarity consider the unitarity gauge where $\mathbf{w} = 0$, which implies $\Sigma = 1$. In this gauge V_μ takes the following form.

$$\begin{aligned} V_\mu &= \frac{i}{2}(gW_\mu^i\sigma^i - g'B_\mu\sigma^3) = \frac{i}{2} \begin{pmatrix} gW_\mu^3 - g'B_\mu & g(W_\mu^1 - iW_\mu^2) \\ g(W_\mu^1 + iW_\mu^2) & -gW_\mu^3 + g'B_\mu \end{pmatrix} \\ &= \frac{i}{2} \begin{pmatrix} \sqrt{g^2 + g'^2}Z_\mu & g\sqrt{2}W_\mu^+ \\ g\sqrt{2}W_\mu^- & \sqrt{g^2 + g'^2}Z_\mu \end{pmatrix} \end{aligned}$$

Where the relationship between the mass and gauge symmetry basis are as follows.

$$W_\mu^+ = \frac{1}{\sqrt{2}}(W_\mu^1 - iW_\mu^2) \quad (\text{A.5})$$

$$W_\mu^- = \frac{1}{\sqrt{2}}(W_\mu^1 + iW_\mu^2) \quad (\text{A.6})$$

$$Z_\mu = c_w W_\mu^3 - s_w B_\mu \quad (\text{A.7})$$

$$A_\mu = s_w W_\mu^3 + c_w B_\mu \quad (\text{A.8})$$

With $c_w = \frac{g}{\sqrt{g^2 + g'^2}}$ and $s_w = \frac{g'}{\sqrt{g^2 + g'^2}}$. Consider the expansion of the terms to be included in the Lagrangian.

$$V^\mu V_\nu = \frac{-1}{4} \begin{pmatrix} \sqrt{g^2 + g'^2} Z^\mu & g\sqrt{2} W^{+\mu} \\ g\sqrt{2} W^{-\mu} & \sqrt{g^2 + g'^2} Z^\mu \end{pmatrix} \begin{pmatrix} \sqrt{g^2 + g'^2} Z_\nu & g\sqrt{2} W_\nu^+ \\ g\sqrt{2} W_\nu^- & \sqrt{g^2 + g'^2} Z_\nu \end{pmatrix} \quad (\text{A.9})$$

$$\text{Tr}[V^\mu V_\nu] = \frac{-1}{2} ((g^2 + g'^2) Z^\mu Z_\nu + g^2 W^{+\mu} W_\nu^- + g^2 W^{-\mu} W_\nu^+) \quad (\text{A.10})$$

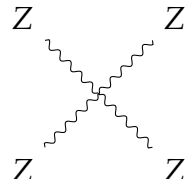
$$\text{Tr}[V^\mu V_\nu] \text{Tr}[V_\mu V^\nu] = \frac{(g^2 + g'^2)^2}{4} (Z^\mu Z_\mu)^2 + g^2 (g^2 + g'^2) (Z^\mu Z^\nu W_\mu^- W_\nu^+) \quad (\text{A.11})$$

$$+ \frac{g^4}{2} (W^{-\mu} W_\mu^+)^2 + \frac{g^4}{2} (W^{-\mu} W^{+\nu} W_\mu^- W_\nu^+) \quad (\text{A.12})$$

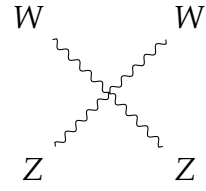
$$\text{Tr}[V^\mu V_\mu]^2 = \frac{(g^2 + g'^2)^2}{4} (Z^\mu Z_\mu)^2 + g^2 (g^2 + g'^2) (Z^\mu Z^\nu W_\mu^- W_\nu^+) \quad (\text{A.13})$$

$$+ g^4 (W^{-\mu} W_\mu^+)^2 \quad (\text{A.14})$$

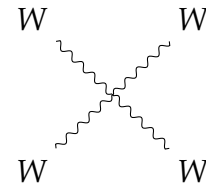
These two terms change the cross section for the vector boson scattering processes at CLIC that involve $ZZ \rightarrow ZZ$, $W^+ W^- \rightarrow ZZ$, $ZZ \rightarrow W^+ W^-$ and $W^+ W^- \rightarrow W^+ W^-$.



$$\subset (\alpha_4 + \alpha_5) \frac{(g^2 + g'^2)^2}{4} \quad (\text{A.15})$$



$$\subset (\alpha_4 + \alpha_5)g^2(g^2 + g'^2) \quad (\text{A.16})$$



$$\subset (\alpha_4 + 2\alpha_5)\frac{g^4}{2} \text{ and } \frac{g^4}{2}\alpha_4 \quad (\text{A.17})$$

A.2. χ^2 Contour Plots for Jet Algorithm Optimisation

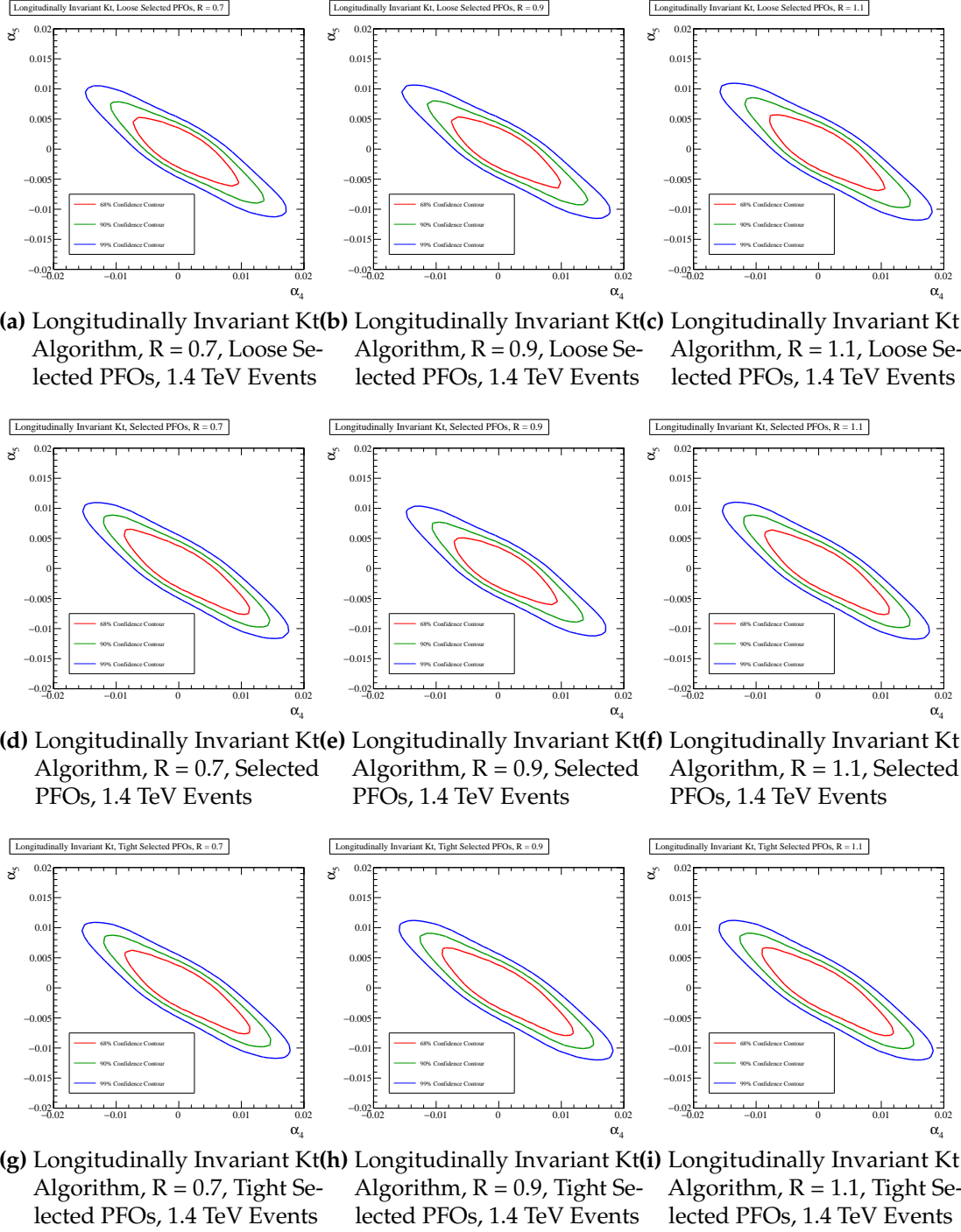


Figure A.1.: χ^2 Sensitivity contours for the $qqqq\nu\nu$ final state arising from a fit to $\cos\theta_{\text{jets}}^*$ at 1.4 TeV for different values of jet reconstruction parameters.

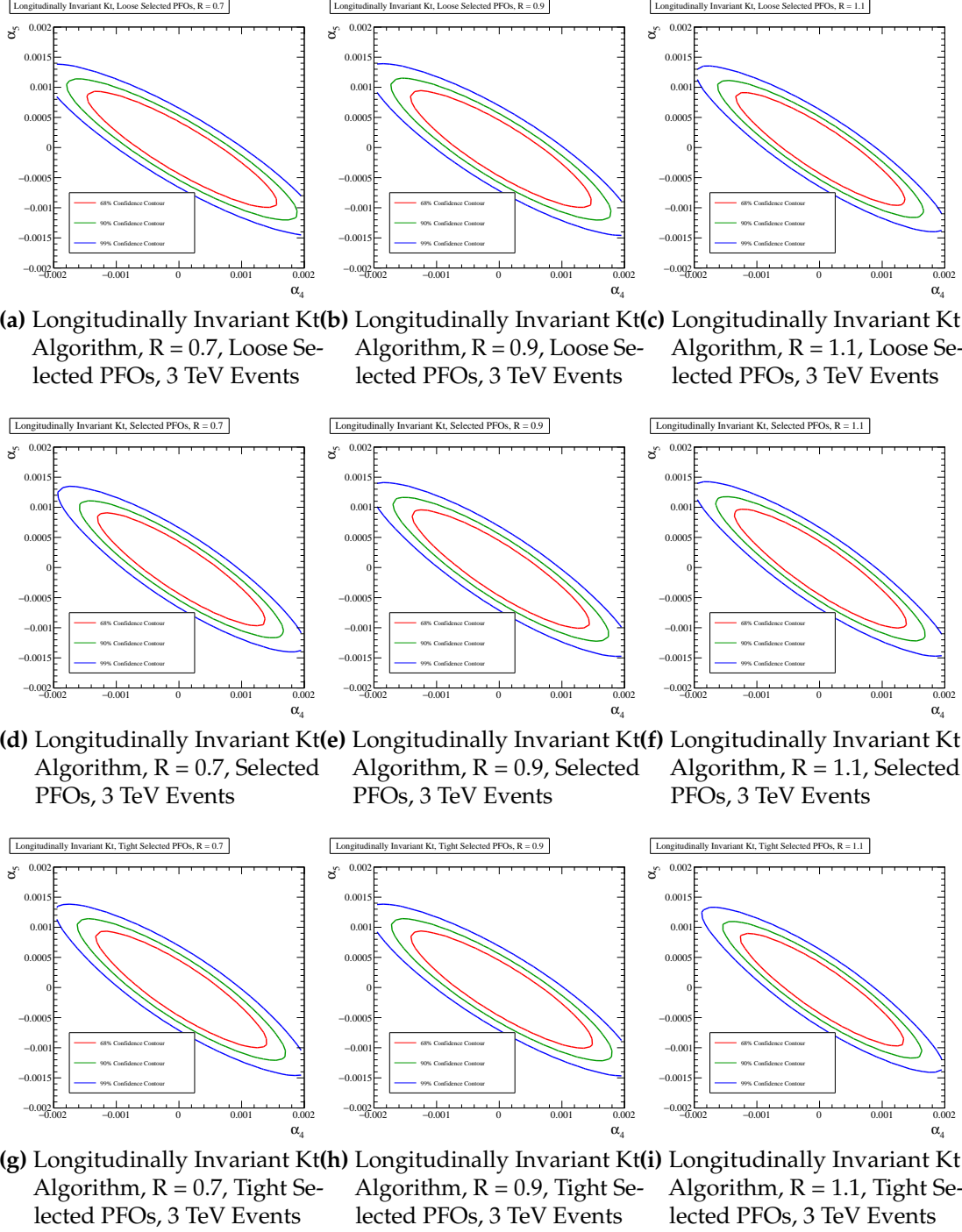


Figure A.2.: χ^2 Sensitivity contours for the $qqqq\nu\nu$ final state arising from a fit to $\cos\theta_{\text{jets}}^*$ at 1.4 TeV for different values of jet reconstruction parameters.

Colophon

This thesis was made in $\text{\LaTeX}2_\epsilon$ using the “hepthesis” class [\[1\]](#).

Bibliography

- [1] Andy Buckley. The hepthesis \LaTeX class.
- [2] C. Patrignani et al. Review of Particle Physics. *Chin. Phys.*, C40(10):100001, 2016.

List of figures

1.1. Energy resolution as a function of photon energy for the nominal ILD detector for both the silicon and scintillator options.	2
1.2. Jet energy resolution as a function of ECal cell size.	4
1.3. Jet energy resolution breakdown as a function of ECal transverse granularity for 45 and 250 GeV jets. Results are given for both the silicon and scintillator ECal options.	5
1.4. Energy resolution as a function of ECal transverse granularity for 100 GeV photons. Results are given for both the silicon and scintillator ECal options.	5
1.5. Jet energy resolution as a function of longitudinal granularity in the ECal.	7
1.6. Jet energy resolution breakdown as a function of ECal longitudinal granularity for 45 and 250 GeV jets. Results are given for both the silicon and scintillator ECal options.	8
1.7. Energy resolution as a function of ECal longitudinal granularity for 100 GeV photons. Results are given for both the silicon and scintillator ECal options.	8
1.8. Jet energy resolution as a function of absorber material in the HCal and physics list.	12
1.9. Jet energy resolution breakdown as a function of HCal absorber material and physics list for 45 and 250 GeV jets.	13
1.10. Jet energy resolution as a function of HCal cell size.	13
1.11. Jet energy resolution breakdown as a function of HCal transverse granularity for 45 and 250 GeV jets.	14

1.12. Energy resolution as a function of HCal transverse granularity for 50 GeV K_L^0	14
1.13. Jet energy resolution as a function of longitudinal granularity in the HCal.	16
1.14. Jet energy resolution breakdown as a function of HCal longitudinal granularity for 45 and 250 GeV jets.	17
1.15. Energy resolution as a function of HCal longitudinal granularity for 50 GeV K_L^0	17
A.1. χ^2 Sensitivity contours for the $qqqq\nu\nu$ final state arising from a fit to $\cos\theta_{\text{jets}}^*$ at 1.4 TeV for different values of jet reconstruction parameters.	23
A.2. χ^2 Sensitivity contours for the $qqqq\nu\nu$ final state arising from a fit to $\cos\theta_{\text{jets}}^*$ at 1.4 TeV for different values of jet reconstruction parameters.	24

List of tables

1.1. Nominal ILD detector model ECal configuration.	3
1.2. Transverse granularity layout of various ECal models considered in this study.	7
1.3. Nominal ILD detector model HCal configuration.	10
1.4. Transverse granularity layout of various HCal models considered. . . .	16